Astron. Nachr./AN **323** (2002) 3/4, 196–202

Waves in magnetic flux concentrations: The critical role of mode mixing and interference

T.J. BOGDAN[1,2,3], C.S. ROSENTHAL[4], M. CARLSSON[4], V. HANSTEEN[4], A. MCMURRY[4], E.J. ZITA[5], M. JOHNSON[5], S. PETTY-POWELL[5], S.W. MCINTOSH[6], Å. NORDLUND[7], R.F. STEIN[8], and S.B.F. DORCH[9]

[1] National Science Foundation, 4201 Wilson Blvd., Arlington, VA 22300 USA
[2] Naval Research Laboratory, 4555 Overlook Ave. SW, Washington, DC 20375 USA
[3] High Altitude Observatory, National Center for Atmospheric Research, P.O. Box 3000, Boulder, CO 80307-3000 USA
[4] Institute of Theoretical Astrophysics, University of Oslo, Box 1029, N-0315 Blindern, Oslo, Norway
[5] The Evergreen State College, Olympia, WA 98505 USA
[6] ESA Research and Scientific Support Department, NASA Goddard Space Flight Center, Greenbelt, MD 20771 USA
[7] NBIfAFG, Københavns Universitet, Juliane Maries Vej 30, DK-2100 København Ø, Denmark
[8] Department of Physics and Astronomy, Michigan State University, East Lansing, MI 48824 USA
[9] The Royal Swedish Academy of Sciences, Stockholm Observatory, SE-133 36 Saltsjöbaden, Sweden

Received 2002 May 10; accepted 2002 July 3

Abstract. Time-dependent numerical simulations of nonlinear wave propagation in a two-dimensional (slab) magnetic field geometry show wave mixing and interference to be important aspects of oscillatory phenomena in starspots and sunspots. Discrete sources located within the umbra generate both fast and slow MHD waves. The latter are compressive acoustic waves which are guided along the magnetic field lines and steepen into N-waves with increasing height in the spot atmosphere. The former are less compressive, and accelerate rapidly upward through the overlying low-β portion of the umbral photosphere and chromosphere ($\beta \equiv 8\pi p/B^2$). As the fast wave fronts impinge upon the $\beta \approx 1$ penumbral "magnetic canopy" from above, they interfere with the outward-propagating field-guided slow waves, and they also mode convert to (non-magnetic) acoustic-gravity waves as they penetrate into the weak magnetic field region which lies between the penumbral canopy and the base of the surrounding photosphere. In a three-dimensional situation, one expects additional generation, mixing and interference with the remaining torsional Alfvén waves.

Key words: stars: oscillations – stars: spots – Sun

1. Introduction

Motivated by recent numerical simulations of waves in spot magnetic field configurations carried out by the group based at the Institute for Theoretical Astrophysics at the University of Oslo, we propose here a novel conceptual framework for interpreting sunspot and starspot oscillations as an interference phenomenon between the three distinct varieties of magneto-atmospheric waves: fast, slow and Alfvénic. The critical advance embodied in these simulations is the abandonment of the traditional one-dimensional and thin fluxtube approaches to modeling sunspot oscillations. While these simpler treatments have permitted a highly-detailed and particularly useful study of the mode-conversion process, they invariably exhibit resonant phenomena as a direct consequence of their low dimensionality and high degree of symmetry. The accumulating observational evidence simply does not support the view that resonant cavities are present in sunspots (Brynildsen et al. 2002).

Multi-dimensional configurations, (1) break many of these implicit symmetries, (2) allow for localized wave sources in space and time, (3) permit the magnetic field to thread the $\beta \approx 1$-layers with various orientations, and (4) provide the opportunity for complex patterns of wave ducting and interaction that are highly variable in both time and location. Unlike their highly symmetrical predecessors, the multi-dimensional configurations are not amenable to analytic treatment. A versatile numerical code to handle such problems is under development, and some preliminary results applicable to a simple two-dimensional spot (slab) magnetic field geometry are described here. They do not take advantage of the full

Correspondence to: tbogdan@nsf.gov

 0004-6337/02/3-408-0196 $ 17.50+.50/0

capabilities of the code to operate in three spatial dimensions and to account for the transfer of radiation based on multi-group methods and incorporating non-LTE level populations. These details are of course crucial for making predictions and for comparisons with observations. Thus in this contribution, we must be content to draw more general conclusions about oscillatory phenomena in spots, while leaving their critical testing and evaluation for a future publication.

2. Numerical simulations

The basic numerical simulations are a simple variant of those introduced by Rosenthal et al (2002). The simulated region represents a portion of the solar atmosphere 1.26 Mm high by 7.90 Mm wide, with translational invariance enforced along the remaining lateral dimension. The base of this computational domain is taken to coincide roughly with the solar surface: it has an initial density and pressure of 2.60 $\times 10^{-7}$ gm cm^{-3}, and 1.13 $\times 10^{5}$ gm cm^{-1} s^{-2}. The overlying atmosphere is isothermal with an effective temperature of 5785 K, a scale-height of 158 km, and a sound speed of 8.49 km s^{-1}. The imposed uniform gravitational acceleration is set at 2.74 $\times 10^{4}$ cm s^{-2}, and the ratio of specific heats is 5/3. The Brunt-Väisälä and acoustic cutoff frequencies are 4.19 mHz and 4.29 mHz, respectively. These atmospheric parameters are identical to those employed in Rosenthal et al (2002).

The imposed magnetic field is potential. There is a strong unipolar magnetic flux concentration located around the 4 Mm mark on the horizontal coordinate scale. A slight amount of reverse polarity field situated about 1 Mm distant on either side. The corresponding magnetic lines of force and the contours of constant plasma-β are shown in Fig 1. Along the bottom boundary, the peak positive and negative vertical magnetic field strengths are 2750 G and -1500 G, while along the upper boundary, the maximum (positive) magnetic field strength is 750 G, and the minimum is 145 G. The computational domain consists of 294 equally-spaced zones in the vertical, and 500 in the horizontal direction. Periodic boundary conditions are enforced on the side walls. A wave-transmitting boundary condition is applied on the upper boundary, and at the lower boundary the normal component of the velocity is specified throughout the simulation. For the examples shown here, u_z is fixed at zero everywhere except between 3.55 Mm and 3.95 Mm where it oscillates sinusoidally with a period of 23.8 s and a peak amplitude of 400 m s^{-1}.

Computational costs and exigencies are the primary motivations which lead us to adopt this particular magneto-atmospheric configuration as a representative scaled-down ($\approx$ 10:1) version of a two-dimensional sunspot. In so far as it is reasonably faithful to the basic morphology of a moderate-sized magnetic flux concentration on a late-type star, the results of this simulation ought to be applicable in a qualitative sense to the behavior of oscillatory disturbances in these structures. A more serious drawback of this simulation than the 10:1 spatio-temporal scaling is the assumption that the fluid motions are isentropic. The negative impact of this restriction is particularly profound for the compressive slow acoustic waves.

3. Results

Figures 1-6 illustrate the key features of the numerical simulation. In these figures we show density fluctuations (Figs 1-3) and the transverse (to the instantaneous magnetic field) fluid motions (Figs 4-6) just after one ($t = 24.7$ s), three ($t = 71.5$ s), and five ($t = 118.3$ s) oscillations of the driving piston. In each figure we also overplot the contours of the plasma-β, and selected magnetic field lines. The $\beta = 1$ contour is thickened relative to the other contours. It separates the low-β plasma of the spot interior from the surrounding high-β regions in the lower left and right quadrants of the domain. The localized piston source resides entirely within the low-β region.

As it oscillates, the piston generates slow and fast magneto-atmospheric waves. The slow waves are essentially acoustic waves that are guided along the prevailing magnetic field. They are most easily discerned by their relative density fluctuations $\Delta\rho/\rho$ shown in Figs 1-3, but they would also be readily visible in parallel (to the instantaneous magnetic field) fluid motions. The fast magneto-atmospheric waves, in contrast, are produced rather inefficiently by the oscillating piston, which makes them difficult to identify from Figs 1-3. Instead, they are better detected by the fluid motions they induce transverse to the magnetic lines of force, as in Figs 4-6, since these motions are largely absent from the slow waves. Only in the vicinity of the steepened N-wave shock fronts, can the slow waves be readily identified in the transverse velocity as thin, slightly curved, striations of red and dark violet in the central light violet region of Figs 5 and 6. Figures 1-3 and 4-6 are therefore complementary in providing a comprehensive visual picture of both the dominant and recessive wave motions present in the simulation.

The slow magneto-atmospheric wave has its fluid motions aligned with the magnetic field and it is compressive. As it moves upward along the magnetic field into regions of lower ambient density its sinusoidal waveform gradually becomes distorted into an N-wave bounded by acoustic shock fronts. The first N-wave is visible in Fig 2 at the leading edge of the slow wave train. The pronounced compression behind the leading edge shocks is reflected in the jagged excursions the iso-β contours make in traversing Figs 2 and 3. They are also distorted, but to a lesser degree, by the rarefaction zones situated in front of the shocks. Since there are negligible magnetic field variations associated with the slow wave, these excursions are entirely due to the pressure variations across the N-wave. It is clear by looking carefully at the sequence of snapshots from Fig 1 to 3 that the slow wave is not entirely contained within the field lines connected to the localized source piston. There is a gradual lateral expansion of the slow wave front to neighboring field lines, although the amplitude of the density fluctuations drops by about one order of magnitude in crossing the last field line connected to the source region. This is seen most clearly in the left lateral extension of the uppermost slow wave present in Fig 3.

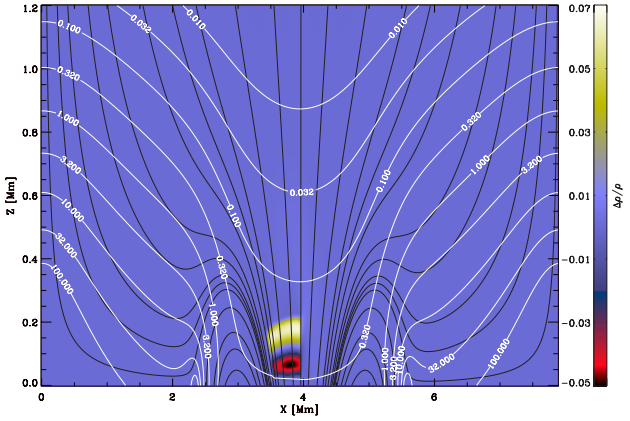

Fig. 1. Density fluctuations, $\Delta\rho/\rho$ at an elapsed time of 24.7 s. Clearly evident is the first sinusoidal compression and rarefaction of the slow magnetic-field-guided acoustic wave. Selected instantaneous magnetic field lines (black lines) and contours of the plasma-β (white lines) are overplotted. See Fig 4 for the transverse velocity at the same elapsed time.

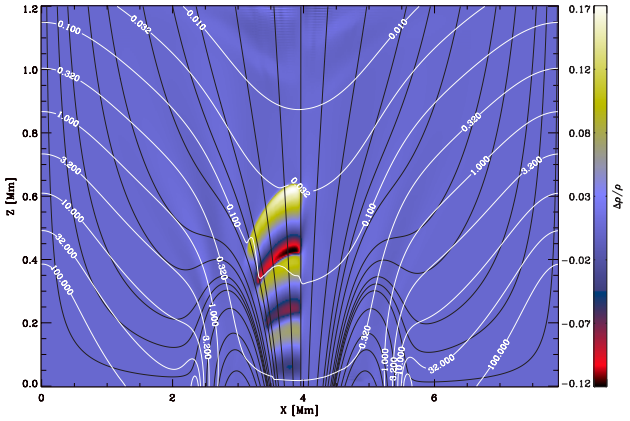

Fig. 2. Density fluctuations at an elapsed time of 71.5 s. Three sinusoidal compressions and rarefactions are now displayed. Notice the increase in the magnitude of the density fluctuations relative to those displayed in Fig 1, and also the gradual steepening of the slow waves with altitude. See Fig 5 for the transverse velocity at the same elapsed time.

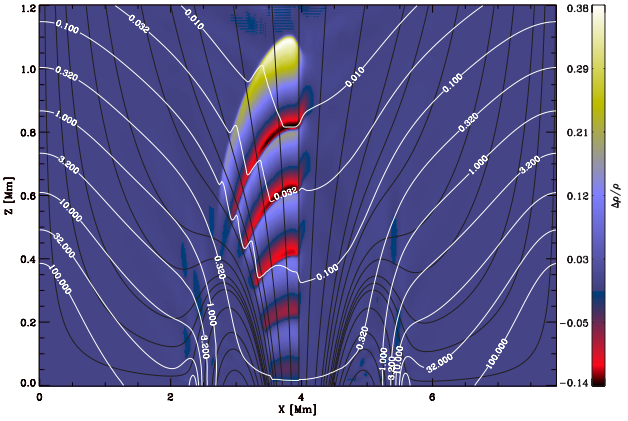

Fig. 3. Density fluctuations at an elapsed time of 118.3 s. Five sinusoidal compressions and rarefactions are now visible. The uppermost disturbances have now fully steepened into N-waves. See Fig 6 for the transverse velocity at the same elapsed time.

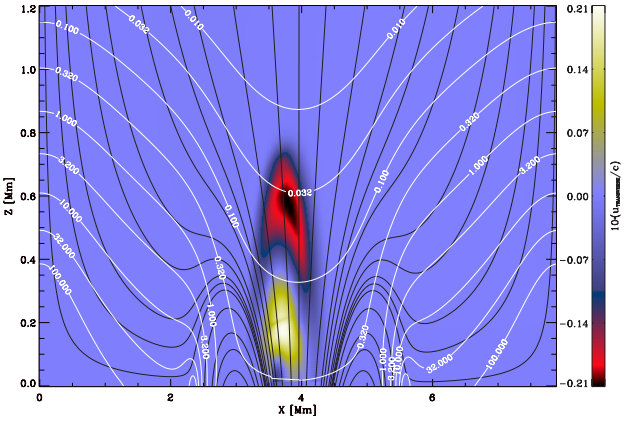

Fig. 4. Velocity component transverse to the magnetic field in units of the sound speed (8.49 km s^{-1}) at an elapsed time of 24.7 s, corresponding to the density fluctuations displayed in Fig 1. This plot principally shows the fast MHD wave. The structure shown here has little correspondence with the slow MHD wave compressions and rarefactions present in Fig 1. Note the factor of 10 enhancement to bring out the color bar labels here, and in Figs 5 and 6.

The fast magneto-atmospheric wave produces somewhat less density perturbation for a given fluid velocity than the slow wave. Density fluctuations associated with the fast waves are present in Figs 1-3, but are swamped by those associated with the slow wave. The choice of the motions transverse to the magnetic field effectively filters out the dominant slow wave and provides an excellent rendering of the recessive fast wave in Figs 4-6. The fast wave also produces motions parallel to the magnetic field, but at a somewhat reduced level relative to those perpendicular to the field. Therefore snapshots of the magnetic-field-aligned velocity look very similar to the fractional density snapshots.

The iso-β contours also serve as contours of constant Alfvén speed because the atmosphere is isothermal. The fast wave fronts therefore accelerate rapidly upward along the center of the magnetic flux concentration along the prevailing Alfvén-speed gradient. The lateral flanks of the wave front decelerate rather gradually as they spread sideways into the regions of lower Alfvén speed which surround the spot. As seen in Figs 5 and 6, this causes the flanks of the fast wave fronts to become convex: the upper portion of the front has traversed a larger lateral distance than has the lower portion. A novel consequence of this configuration is that the high-β regions surrounding the spot see the fast waves propagating *downward* as they pass across the magnetic canopy.

The $\beta \approx 1$ magnetic canopy is the principal site of wave mixing and conversion. Fig 5 indicates that significant portions of the fast wave fronts arrive at the canopy almost simultaneously. Proceeding to Fig 6, one sees that they pass

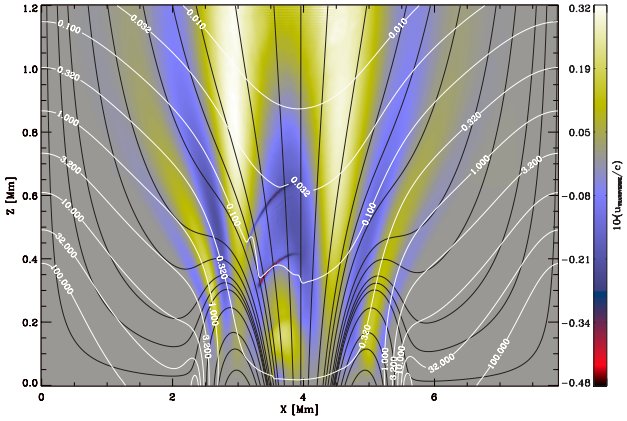

Fig. 5. Velocity component transverse to the magnetic field in units of the sound speed at an elapsed time of 71.5 s (cf. Fig 2). Three oscillatory cycles are visible with the orientation of violet hues leading yellow. The steepened N-waves of Fig 2 can now be detected as thin striations of red within the central violet region.

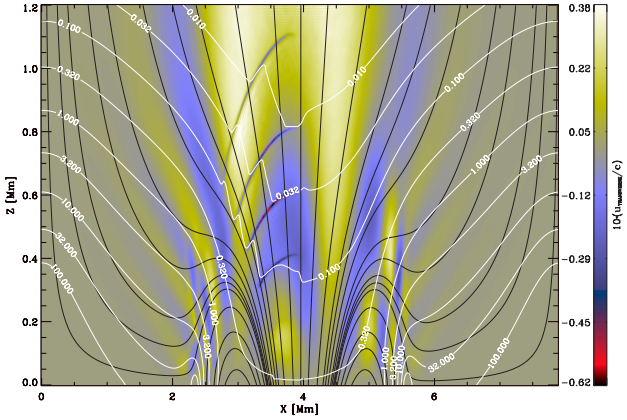

Fig. 6. Velocity component transverse to the magnetic field in units of the sound speed (8.49 km s^{-1}) at an elapsed time of 118.3 s (cf. Fig 3). The steady lateral outward propagation of the fast waves is readily apparent, as are the striations associated with the acoustic shocks.

seamlessly across this transition layer converted smoothly to the high-β fast wave. The high-β fast magneto-atmospheric wave is essentially an acoustic-gravity wave which is unaffected by the (weak) magnetic field. In an isothermal atmosphere the frequency (ω), horizontal ($k_\perp$), and vertical ($k_\parallel$) wavenumbers satisfy the familiar dispersion relation

$$k_\parallel^2 = \frac{\omega^2 - \Omega^2}{c^2} + k_\perp^2 \left(\frac{N^2}{\omega^2} - 1 \right) , \qquad (1)$$

where Ω and N are the acoustic cutoff and Brunt-Väisälä (buoyancy) frequencies, and c is the sound speed. For our piston driving frequency of $\omega/2\pi = 42$ mHz, Eqn (1) is essentially acoustic,

$$k_\parallel^2 \approx \frac{\omega^2}{c^2} - k_\perp^2 . \qquad (2)$$

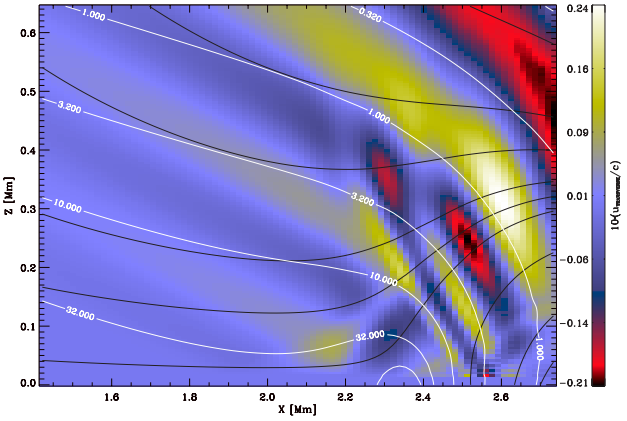

Fig. 7. Detail from Fig 6 showing the region surrounding the $\beta = 1$ canopy surface, and the motions perpendicular to the magnetic lines of force. The low-β fast waves impinge on the canopy from above, and are now seen to generate *both* slow and fast high-β waves. The slow Alfvén-like waves are represented by the two thin inclined yellow-violet fronts between the $\beta = 3.2$ and the $\beta = 10$ contours. The fast acoustic-gravity waves are the very broad and more highly inclined undulations seen to the left of $x = 2.2$ Mm.

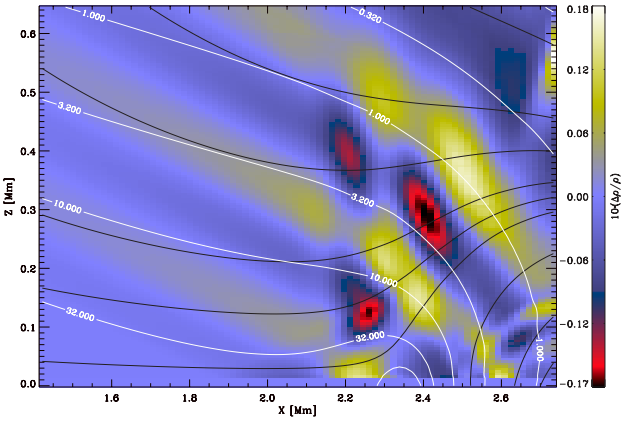

Fig. 8. Detail from Fig 3 showing 10 ($\Delta\rho/\rho$). Note the absence of any structure associated with the slow Alfvén-like waves seen in Fig 7. The fast acoustic-like waves are again obvious to the left of $x = 2.2$ Mm.

It is hard to see the conversion to the high-β slow magneto-atmospheric wave in Fig 6. This object is nearly indistinguishable from an Alfvén wave in character, and will be propagated strictly along the magnetic lines of force. The optimal location for seeking fast-to-slow wave conversion is therefore between the altitudes of 200 km and 400 km, where the magnetic field lines are both perpendicular to, and subsequently diverge away from, the $\beta = 1$ surface.

Figs 7 and 8 show detail from Figs 6 and 3, respectively, in the vicinity of this optimal location for fast-to-slow mode conversion. Above the canopy surface one sees the impinging low-β fast waves clearly in the transverse velocity (Fig 7), and between the $\beta = 3.2$ and $\beta = 10$ contours are the first emergent slow, Alfvén-like, waves. As the Alfvén

speed decreases outward along the magnetic field lines, the wavelength of these slow waves also decreases and they are rapidly lost to the numerical viscosity and resistivity of the finite computational grid. For solar dissipation levels, they would instead dissipate by phase-mixing. A comparison of Fig 7 with Fig 8 confirms our identification of these objects as incompressible, transverse, fluctuations. Such a comparison likewise helps to identify the high-β fast waves as the more highly-inclined, relatively weak, gradual undulations present in the left halves of these two figures. The first fast-wave front to emerge from the canopy is seen to intersect the lower boundary of the computational domain in the vicinity of $x = 2.0$ Mm. To the right of this point, one may just discern the upward continuation of this wave front which has already reflected off the lower boundary. It is difficult to follow the extension of this front, or reflections associated with subsequent fronts, much higher in the atmosphere owing to their interference with the later portions of the emitted wave train. In a similar vein, one may notice that the region surrounding the $\beta = 1$ canopy exhibits complicated structures which are not obviously categorized as being compressible or incompressible, nor polarized parallel or perpendicular to the magnetic field. This reflects the confusion the incoming fast waves experience when the acoustic and Alfvén speeds are difficult to distinguish.

In Fig 8 it is also just possible to discern the outer edge of the second low-β slow N-wave front. The front starts just below the upper right corner of the plot and extends down to the point $x = 2.6$ Mm and $z = 0.3$ Mm, where it gets lost in the canopy region.

It is thus quite clear that the region displayed in Figs 7 and 8 is subject to a fair amount of interference between various wave trains. Above the $\beta = 1$ canopy there is interference between the piston-generated slow and fast wave trains. The former propagate from right to left upward *along* the magnetic field lines; the latter move from right to left downward *across* the field. Below the canopy, the situation is even more complicated. We have both the mode-converted fast and slow wave trains emerging from the canopy, at distinct locations and propagating in different directions, and the fast waves reflected from the lower boundary. It therefore comes as no surprise that it would be a monumental undertaking to infer the behavior of the waves emitted from the source piston based simply on limited knowledge of the oscillations at a specified altitude in the atmosphere.

The point is illustrated by Figs 9 and 10, which display the fluctuations present at a fixed altitude of 150 km. In Fig 9, we show the density fluctuation, $\Delta\rho/\rho$, and in Fig 10 we show the vertical velocity u_z in units of the sound speed. Both are enhanced by a factor of 10 to bring out the labels on the color bar scale. In a naive sense, the former are representative of hypothetical intensity fluctuation ($\sim \Delta I/I$) time series, while the latter mimic Doppler velocities from a vantage point looking down on the simulation from above. Notice that the images of the full computational domain displayed in Figs 1-6 correspond to the three epochs $t = 24.7$ s, 71.5 s, and 118.3 s.

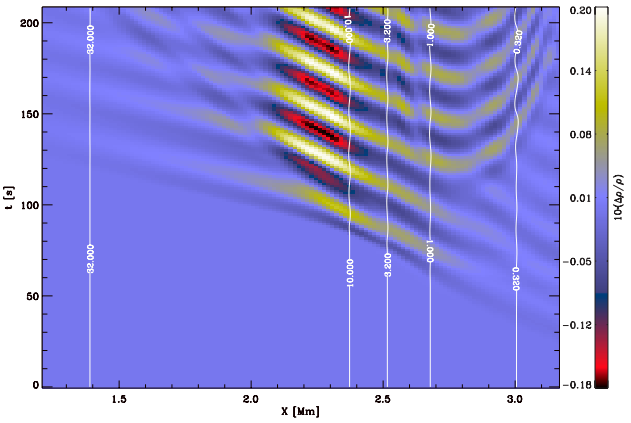

Fig. 9. Density fluctuations $\Delta\rho/\rho$ obtained at a fixed altitude of 150 km, as a function of elapsed time. The lateral location of the contours of constant plasma-β are indicated by white lines. See Fig 10 for the corresponding vertical velocity.

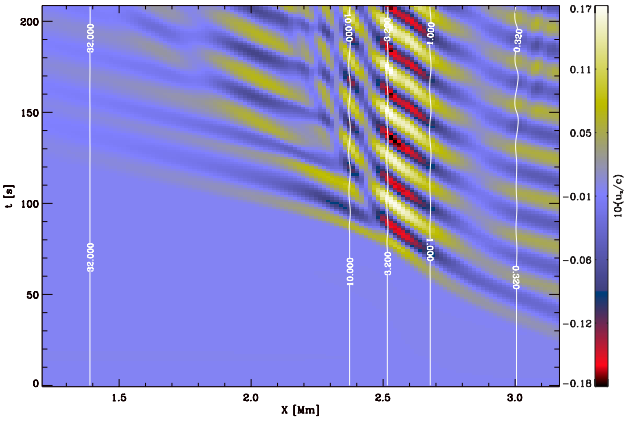

Fig. 10. Vertical component of the velocity obtained at a fixed altitude of 150 km, as a function of elapsed time. See Fig 9 for the corresponding density fluctuations in the same format.

It is instructive to sort out the individual wave trains which feature in this pair of figures. The first (in time) outward-propagating fast wave oscillation presents a thin continuous structure coincident in density (dark violet) and velocity (yellow), which traverses the entire horizontal extent of both plots. As this structure crosses the $\beta = 1$ magnetic canopy its apparent horizontal phase speed along the $z = 150$ km atmospheric layer abruptly increases. This is simply a geometrical projection effect (see Figs 7 and 8), owing to the large inclination with respect to the vertical of the transmitted high-β fast wave (i.e., acoustic-gravity wave) fronts.

Fig 10 also confirms that the impinging low-β fast wave is partially converted into transmitted slow (quasi-Alfvénic) waves in the high-β plasma. This slow wave train is represented by the sequence of tight-packed arcs between $x = 2.2$ Mm and 2.5 Mm in the plot of u_z. It is absent in Fig 9 because there are no density fluctuations associated with this transverse magnetic oscillation. Notice the interesting inter-

ference pattern that develops on the high-β side of the magnetic canopy due to the coherent superposition of the individual u_z fluctuations associated with the transmitted fast and slow wave trains.

With the arrival of the third fast wave oscillation at the magnetic canopy ($t \approx 105$ s), a new series of waves are now observed to be reflected back into the low-β plasma *and* transmitted a very short distance into the low-β region. These are best seen in the density fluctuations as a nested sequence of parabolic arcs to the right of $x = 2.5$ Mm in Fig 9. They are just barely discerned in the upper right corner of Fig 10. This indicates that they are basically compressive acoustic oscillations with fluid motions aligned with the prevailing magnetic field. They do not produce a sensible u_z until the field becomes more favorably (less horizontally) oriented on the right side of the region depicted in Figs 9 and 10.

These waves are not, in fact, associated with the mode-mixing of the impinging low-β fast wave at the intersection of the $z = 150$ km surface and the $\beta = 1$ magnetic canopy. Rather, they are generated by the passage of the outward propagating fast waves across the footpoints of the magnetic field lines. Since the footpoints are anchored at the boundary, the pressure fluctuations associated with the fast wave generate field-aligned motions which subsequently propagate up along the magnetic loops as magnetic-field-guided acoustic waves. This ancillary wave emission from the boundary is appreciable where the gas and magnetic pressures are comparable.

The magnetic-field-guided acoustic waves generated in this manner give the visual appearance of upward propagating arcs, as partially depicted in the lower right corners of Figs 7 and 8. The sequential arrival of these waves at the $z = 150$ km atmospheric layer naturally produces the nested parabolic structures visible in Fig 9, and correctly accounts for their delay relative to the other waves trains discussed earlier. It is a pure coincidence that the first of these waves arrives in the vicinity of the $\beta = 1$ magnetic canopy.

The horizontally-propagating fast wave that is responsible for the generation of the boundary acoustic waves continues its lateral progression after passing through the closed field region. On its emergence from this structure into the high-β surroundings it subsequently reforms as a horizontally-propagating Lamb wave. The upward extension of these Lamb wave fronts through the $z = 150$ km layer gives rise to a series of inclined linear structures visible in Fig 9 between $x = 1.4$ Mm and 2.2 Mm. The interference pattern present in the upper left quadrant of Fig 9 therefore results from the superposition of fast waves which have been emitted from *different* portions of the $\beta = 1$ magnetic canopy. This can ultimately be traced back to the convex fast wave fronts present in Figs 5 and 6. Consistent with the Lamb wave having $|u_x| \gg |u_z|$, this interference feature is absent from Fig 10.

4. Summary

Our brief discussion of Figs 1-10 has brought out a number of important points concerning the general nature of wave propagation in two-dimensional magneto-atmospheres. Despite several idealizations present in these simulations, our findings are broadly relevant for studies of oscillatory phenomena in starspots, sunspots, and generic stellar surface magnetic flux concentrations.

We have seen very clearly the critical role played by the "magnetic canopy surface", defined here as where the Alfvén and sound speeds are comparable, or equivalently, where the plasma-β is of order unity. This surface separates regions of high- and low-β plasma. Within these distinct regions the fast- and slow magneto-atmospheric waves are readily distinguished one from the other, but such an unambiguous identification does not extend *across* the canopy, where the waves of each side are mixed and lose their respective identities. The canopy is therefore the quintessential site for conversion between the different waves.

This fact was of course well-appreciated by very many one-dimensional treatments of sunspot oscillations (see references in Bogdan 2000). What is new here are the novel facets introduced by the curvature of this surface and the variations of the angle between the normal to the surface and the local magnetic field. This can inhibit or promote the conversion to a particular variety of wave, while at the same time allowing wave trains emanating from different portions of the canopy to overlap and interfere at various locations in the surrounding high- and low-β plasmas. A visual inspection of Figs 9 and 10 is sufficient to appreciate the complex mixing around the $\beta = 1$ layer. Not only do canopy surfaces create additional wave varieties, but localized sources do the same. The vertical motion of the driving piston was selected to produce slow low-β acoustic waves, but we have seen that low-β fast waves are also created, which then subsequently convert to other waves upon encountering the canopy. This fascinating interplay between mode mixing and interference therefore emerges from our discussion as the essential aspect of wave propagation in sunspots and starspots.

Those who acquire and interpret observations can capitalize upon the critical role played by the "magnetic canopy surface" in orchestrating this complicated interplay (e.g., McIntosh et al. 2001). One gains a first advantage by knowing whether the relevant observations obtain on the high- or low-β side of this surface. A second advantage follows if one can further determine the general shape and relation to the prevailing magnetic field of the canopy extensions which pass nearest to the site of the observations.

For example, consider the phenomenon of running penumbral waves (RPWs). The well-known difficulty of detecting these objects at photospheric levels may well be explained by supposing, merely for the sake of argument, that these waves are related in some fashion to the low-β slow wave train shown in Fig 3. The lack of any appreciable extension of these waves into lower atmospheric layers is prohibited by the intervening $\beta = 1$ canopy. This is a fairly trivial observation, but the analysis presented in this contribution clearly indicates many other more sophisticated, and potentially powerful, lines of reasoning which may help in sorting out the bewildering array of properties of oscillations in and around magnetic flux concentrations. Lack of space prohibits

us from taking this discussion further. The interested reader should consult a forthcoming paper by Bogdan et al. (2002).

Acknowledgements. TJB expresses his sincere thanks to Spiro Antiochos and the Naval Research Lab for their kind support and hospitality offered during his assignment with the National Science Foundation. He also is grateful to Dr. Richard Behnke for his encouragement and interest in this research activity.

References

Bogdan, T.J.: 2000, SoPh 192, 373
Bogdan, T.J., et al.: 2002, ApJ, in preparation
Brynildsen, N., et al.: 2002, SoPh, in preparation
McIntosh, S.W., et al.: 2001, ApJ 548, L237
Rosenthal, C.S., et al.: 2002, ApJ 564, 508